International Journal of Nanomedicine

Dovepress
Taylor & Francis Group

Open Access Full Text Article

ORIGINAL RESEARCH

Engineered Biomimetic Nanomicelles Target Inflammation in Sepsis-Associated Acute Lung Injury by Scavenging ROS and Reprogramming Macrophages

Quan Li[1,*], Haijun Sun[1,*], Xinjing Zhang[2,*], Yani Chen[1], Zhifeng Wu[1], Maohong Xia[1], Lu Sun[1], Weigang Shi[1], Zhaorui Sun[3], Wei Li[4], Lili Ding[1]

[1]Intensive Care Unit, Jiangsu Province (Suqian) Hospital, Suqian, Jiangsu, 223899, People's Republic of China; [2]Pulmonary and Critical Care Medicine, Jiangsu Province (Suqian) Hospital, Suqian, Jiangsu, 223899, People's Republic of China; [3]Department of Emergency Medicine, Jinling Hospital, Medical School of Nanjing University, Nanjing, Jiangsu, 210093, People's Republic of China; [4]Department of Emergency Medicine, The First Affiliated Hospital with Nanjing Medical University, Nanjing, Jiangsu, 210029, People's Republic of China

*These authors contributed equally to this work

Correspondence: Wei Li; Lili Ding, Email liwei5477@jsph.org.cn; lzwlk20150221@163.com

Background: Sepsis-associated acute lung injury (SALI) has high mortality, largely driven by a damaging cycle of oxidative stress and inflammation, with a lack of effective treatments. To address this, a novel biomimetic nanodrug was developed. It uses an amphiphilic copolymer (PT) to encapsulate the antioxidant/anti-inflammatory agent carnosic acid (CA), forming PT@CA micelles. These micelles are then coated with M2 macrophage membranes (MM) to create MM@PT@CA. Compared to traditional liposomes, the macrophage membrane has better inflammatory targeting and biological safety.

Methods: The PT copolymer was synthesized by grafting thioctic acid onto polylysine. CA was encapsulated via anti-solvent precipitation to form PT@CA, which was subsequently coated with M2 macrophage membranes via co-extrusion to yield the final bionic nanomicelle, MM@PT@CA. The system's ROS-responsive drug release, antioxidant, and antibacterial activities were characterized. Its biocompatibility, ability to scavenge cellular ROS, anti-inflammatory effects, and promotion of M2 macrophage polarization were assessed in vitro. Therapeutic efficacy was further evaluated in a mouse model of sepsis-induced lung injury.

Results: MM@PT@CA demonstrated significant multifunctional efficacy across a series of experiments. In vitro, it scavenged DPPH and ABTS radicals by 74.07% and 91.47%, respectively, and inhibited the growth of Staphylococcus aureus and Escherichia coli. It was efficiently taken up by cells and accumulated at inflammatory sites. Moreover, it exhibited excellent biocompatibility, remarkably restoring cell viability under oxidative stress from 48.70% to 93.85% while down-regulating pro-inflammatory factors. In vivo, MM@PT@CA treatment reduced apoptosis from 28.79% to 5.49%. Notably, the progression of SALI was effectively halted, which was attributed to its ability to modulate macrophage polarization and inhibit the pro-inflammatory cytokine storm.

Conclusion: The developed bionic nanomicelle targets inflammation, combats infection and oxidative stress, and ultimately alleviates SALI. These features highlight MM@PT@CA promising therapeutic potential for the treatment of SALI.

Keywords: acute lung injury, biomimetic nanomicelles, ROS scavenging, macrophage reprogramming, carnosic acid

Introduction

Sepsis, a syndrome of dysregulated immune response triggered by systemic infection, frequently leads to acute lung injury.[1,2] While current clinical management primarily relies on mechanical ventilation and broad-spectrum antibiotics,[3] complications such as ventilator-associated lung injury and antimicrobial resistance[4] underscore the urgent need to develop novel targeted therapies. The pathogenic mechanisms of sepsis-associated acute lung injury (SALI) involve multidimensional pathological interactions: Pathogen associated molecular patterns (PAMP) and damage associated

Received: 30 September 2025
Accepted: 17 December 2025
Published: 26 December 2025

Graphical Abstract

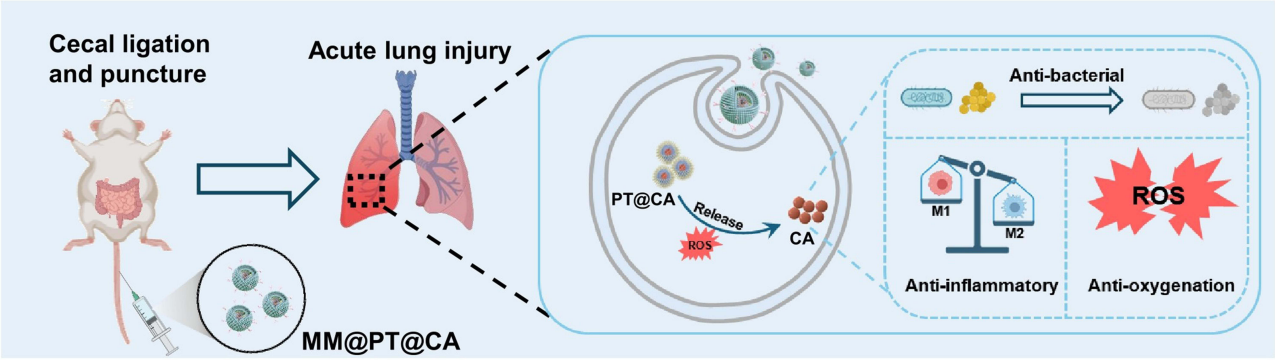

molecular patterns (DAMP) activate immune cells via pattern recognition receptors (PRRs), triggering a pro-inflammatory cytokine cascade that culminates in a "cytokine storm".[5–7] Concurrently, the dysregulation of compensatory anti-inflammatory responses leads to immune paralysis, which exacerbates tissue repair impairment. Notably, oxidative stress and inflammatory responses form a bidirectional vicious cycle during the progression of sepsis-associated acute lung injury, where overactivated neutrophils generate excessive reactive oxygen species (ROS) through respiratory bursts, directly damaging pulmonary parenchymal cells and amplifying inflammatory cascades via activation of NF-κB,[8] while the sustained inflammatory microenvironment further exacerbates mitochondrial dysfunction, leading to ROS accumulation.[9]

Oxidative stress is one of the pathogenic mechanisms of sepsis. Recently, numerous strategies have been developed to target the clearance of oxidative stress. For example, Au/CeO_2 nanozymes, which exhibit five enzymatic activities, participate in oxidative stress homeostasis and immune regulation and protect against sepsis-induced inflammation and organ dysfunction.[10] Polyphenol-copper nanozymes (Cu-CA NZs) alleviate excessive endoplasmic reticulum stress in the liver by mediating the eIF2α/ATF4/CHOP pathway, thereby treating sepsis-induced acute liver injury.[11] However, nanozymes carry the risk of metal toxicity[12] and their prevalent peroxidase-like activity may exacerbate hydroxyl radical generation, causing damage to healthy tissues. Micelles, known for their high drug-loading capacity, are widely used to deliver therapeutics for oxidative stress injuries. For instance, resveratrol encapsulated in polycaprolactone-polyethylene glycol (PCL-PEG) micelles has been used for acute lung injury treatment.[13] Nevertheless, conventional micelles lack responsive release mechanisms, which limits their ability to rapidly mitigate inflammation. Dexamethasone (Dex), a potent anti-inflammatory drug, is frequently encapsulated in micelles to study its therapeutic effects in lung injury. However, systemic administration of Dex remains a significant challenge owing to its toxic side effects. Carnosic acid (CA), a natural phenolic diterpenoid compound, demonstrates potential in treating pulmonary inflammatory diseases owing to its notable antibacterial, anti-inflammatory, and antioxidant activities.[14,15] Furthermore, CA exhibited excellent biocompatibility, making it suitable for the treatment of SALI. Additionally, the complex physiological barriers of the lungs often result in insufficient accumulation of conventional nanomedicines at lesion sites,[16] underscoring the critical need to develop delivery systems with active targeting capabilities.

In recent years, cell membrane-coated nanoparticles have attracted significant research interest due to their biomimetic properties. Compared with traditional chemical modification strategies, natural cell membranes not only prolong the blood circulation time of nanoparticles but also enable targeted delivery through membrane surface proteins. However, the translation of macrophage membrane-based delivery systems still faces challenges, including scalability and immune compatibility. To address these issues, this study employed an immortalized M2-polarized macrophage cell line as a stable and reusable source of cell membranes. Combined with a standardized extrusion preparation process, this approach significantly improved the production consistency and scalability of membrane-coated nanoparticles. Moreover,

the endogenous M2 macrophage membrane exhibits inherent biocompatibility, which helps mitigate the risk of allogeneic immune responses. The retained chemokine receptors and anti-inflammatory protein components on the membrane further confer dual functions to the nanoparticles: active accumulation at inflammatory sites[17] and immunomodulation.[18] Building on this, the study coated M2 macrophage membranes onto ROS-responsive micellar cores to achieve efficient and controlled drug release at inflammatory sites, thereby synergistically enhancing the therapeutic efficacy.

In this study, we engineered a biomimetic M2 macrophage membrane (MM)-coated ROS-responsive nanomicelle system (MM@PT@CA) through triple-functional integration. The core structure (PT) employed polylysine (PLL) covalently grafted with thioctic acid (TA), leveraging its amphiphilic properties to self-assemble into micelles that efficiently encapsulate the hydrophobic drug CA within their hydrophobic cores (PT@CA). Simultaneously, TA moieties confer ROS responsiveness through dynamic disulfide bonds, enabling targeted drug release in high-ROS microenvironments that are characteristic of pulmonary injury lesions. Furthermore, surface cloaking with membranes derived from M2-polarized macrophages equips nanomicelles with innate immune evasion capabilities, while capitalizing on membrane-retained chemokine receptors and anti-inflammatory proteins. This dual-functional membrane engineering enables chemokine gradient-driven active targeting to inflammatory sites, effectively overcoming pulmonary physiological barriers, and enhancing lesion accumulation efficiency. This integrated "carrier-responsiveness-targeting" trinity design synergistically addressed the pharmacokinetic limitations of CA and pulmonary targeting challenges, thereby establishing a systematic solution for clinical translation (Figure 1).

Methods and Materials

Materials

All experimental materials were sourced from certified suppliers with specified purity grades and biological activity certification. RAW264.7 murine macrophages were procured from Procell Life Sciences and Technology (Wuhan, China). Key chemical components, including carnosic acid (CA, 98%, AR grade), thioctic acid (TA, 98%, AR grade), poly-L-lysine (PLL, 98%, AR grade), and absolute ethanol (99.5%, AR grade), were obtained from Macklin (Shanghai, China), and the coupling agents NHS (98%, AR) and EDC (98%, AR grade) were acquired from Aladdin (Shanghai, China). Lipopolysaccharide (LPS) purchased from Sigma-Aldrich (St. Louis, MO, USA). Essential detection kits, calcein-AM/PI viability assay, CCK-8 proliferation kit, and DCFH-DA ROS detection kit were purchased from Beyotime Biotechnology (Shanghai, China). Cellular staining reagents (Hoechst 33342, DAPI, and FITC-phalloidin) and hydrogen peroxide quantification kits were purchased from SolarBio (Beijing, China). Cytokine profiling was performed using ELISA kits for TNF-α, Arg-1, IL-1β, and IL-10 (MLbio, Shanghai, China). Macrophage polarization analysis was performed using PE/Cy7 anti-CD206 and FITC anti-CD86 antibodies from Proteintech (Wuhan, China).

Synthesis of PT and PT@CA

Preparation of PT: The polymer was synthesized according to a previously reported method[19] with modifications. Briefly, One-gram thioctic acid (TA) was dissolved in 100mL of 50% ethanol solution. The carboxyl groups of TA were activated by adding EDC (25 mM) and NHS (50 mM), followed by stirring at room temperature for 30 min. Subsequently, 0.25 g poly-L-lysine (PLL) was gradually mixed with the activated TA solution and allowed to react continuously for 18 h to achieve TA grafting. Residual ethanol was removed by rotary evaporation, and unreacted TA was eliminated by centrifugation. The collected PT solution was freeze-dried for subsequent use.

Preparation of PT@CA: The micelles were prepared using the anti-solvent precipitation method, following the procedure reported by Ameneh Elmizadeh et al[20] with minor modifications. Briefly, 1 mL of an ethanol solution containing PT (10 mg) and TA (0.5 mg) was added dropwise into 10 mL of distilled water under magnetic stirring at 1000 rpm for 30 min. The ethanol was then evaporated using a rotary evaporator (temperature: 40 °C, pressure: 0.1 MPa) for 30 min. The volume lost due to ethanol evaporation was replenished by adding distilled water. Finally, the formed micelles were stored at 4 °C.

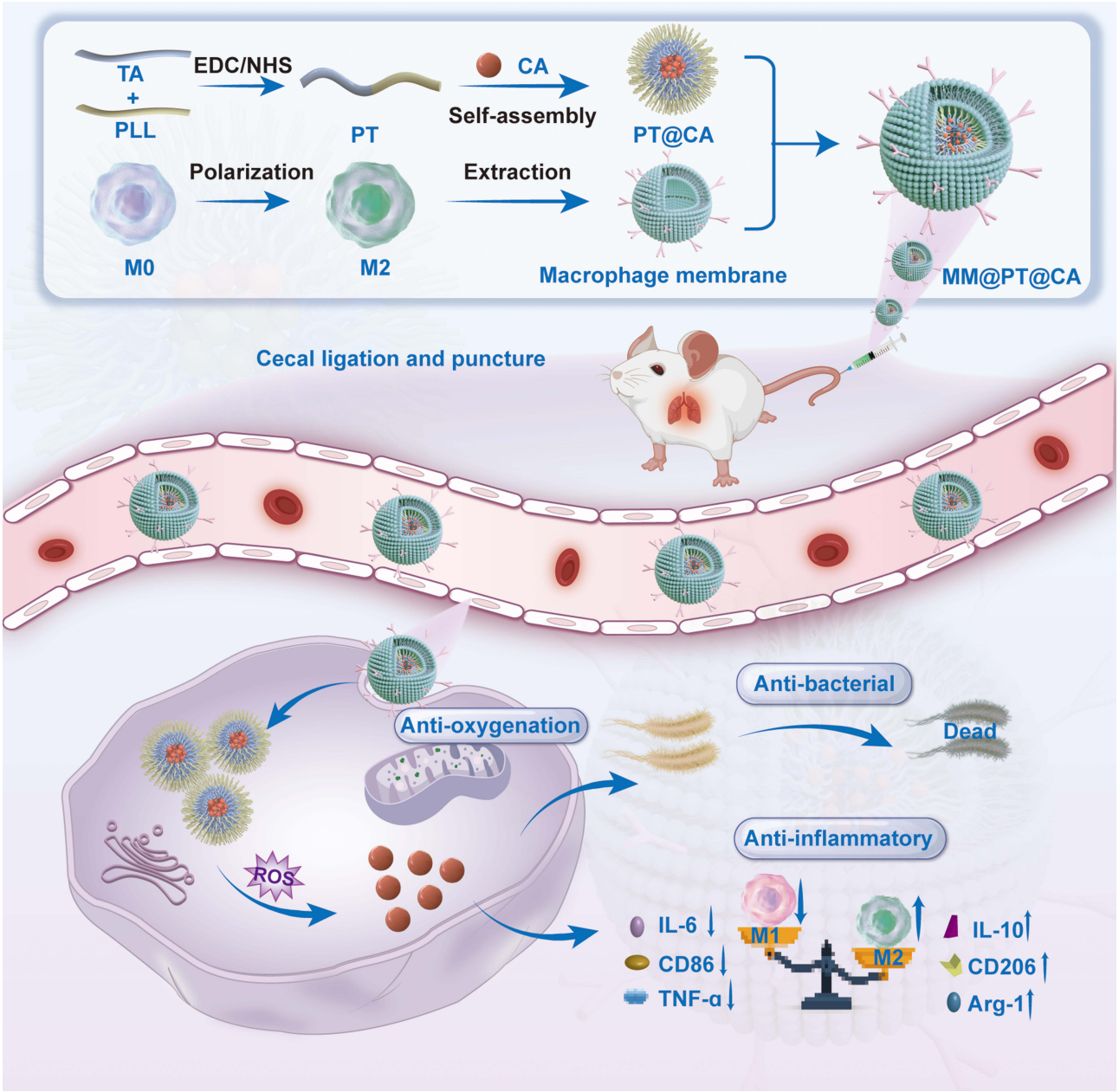

Figure 1 The synthetic route of MM@PT@CA and the mechanism of action in the treatment of SALI. The arrows indicate the increase (upward arrows) or decrease (downward arrows) of the corresponding cytokine expression.

Isolation of M2 Macrophage Membranes

The method was adapted from previous studies[21,22] with minor modifications. Briefly, RAW264.7 cells were induced with IL-4 (20 ng/mL) for 24h to obtain M2-type macrophages and the M2-type macrophages were lysed by sonication (10 min at 4 °C) in hypotonic buffer. After removing Cellular debris by centrifugation (10,000 ×g, 30 min, 4 °C), the supernatant was subjected to ultracentrifugation (150,000 ×g, 1 h, 4 °C) to isolate M2 macrophage membrane (MM). The obtained MM were resuspended in PBS and stored at −80°C for subsequent use.

Preparation of MM@PT@CA

The isolated M2 macrophage membrane (1 mg/mL, 500 μL) was thoroughly mixed with PT@CA (1 mg/mL, 500 μL) in deionized water. The resulting mixture was incubated at room temperature for 1 h to facilitate membrane fusion.

Subsequently, the mixture was co-extruded through a 200 nm polycarbonate membrane to ensure a uniform coating. Finally, the extruded solution was centrifuged at 14,000 ×g for 10 min to harvest MM@PT@CA nanoparticles.

Characterization of MM@PT@CA

The successful grafting of TA onto PLL was verified by Fourier-transform infrared (FTIR, SHIMADZU IRTracer-100, Japan) and proton nuclear magnetic resonance (^{1}H NMR, Bruker AVANCE III HD 600, Germany) spectroscopy. The loading efficiency of CA was determined by ultraviolet-visible spectrophotometry. The particle size distribution and zeta potential of MM@PT@CA nanoparticles were measured by dynamic light scattering (DLS, Malvern Panalytical, Zetasizer Pro, UK). The morphology of MM@PT@CA was examined by transmission electron microscopy (TEM, JEOL JEM-F200, Japan). Fluorescence microscopy was employed to confirm the successful coating of MM on the outer layer of PT@CA micelles.

In Vitro Release Behavior of MM@PT@CA

To investigate the H_2O_2-responsive release behavior, the in vitro release of CA was monitored by dialysis. MM@PT@CA (1 mL) was placed in dialysis bags (MWCO 3500 Da) and immersed in 10 mL of PBS (pH 7.4), with or without 10 mM H_2O_2. The Samples were then incubated at 37 °C on an orbital shaker at 90 rpm for 12 h. To maintain a constant volume, an equal amount of fresh release medium was added immediately after collecting 1 mL of the sample at each designated time point. The cumulative release of CA was quantified by ultraviolet-visible spectrophotometry.

Antioxidant Properties of MM@PT@CA

1,1-diphenyl-2-picryl-hydrazyl radical (DPPH) radical scavenging assays PT, PT@CA, and MM@PT@CA were performed separately. DPPH solution was mixed with each material at a 1:1 volume ratio. The mixtures were incubated in the dark for 30 min, and absorbance was measured at 517 nm using a UV-Vis spectrophotometer.

The 2,2′-Azino-bis (3-ethylbenzothiazoline-6-sulfonic acid) (ABTS) radical scavenging assay was performed following the same protocol as the DPPH assay, with absorbance measurements recorded at 734 nm. The radical-scavenging ratio was calculated using the following formula:

$$\text{Radical scavenging ratio}(\%) = \frac{A_{control} - A_{sample}}{A_{control}} \times 100\%$$

Where A_{control} and A_{sample} are the absorbance values of the DPPH/ABTS radical solutions in the absence and presence of test materials, respectively.

H_2O_2 scavenging assay All reaction tubes were pretreated with 100 mM H_2O_2, followed by the addition of PT, PT@CA, or MM@PT@CA (100 μL each), with blank controls established in parallel. Residual H_2O_2 content was quantified at various time points using a commercial H_2O_2 detection kit, from which the H_2O_2 scavenging ratio was calculated.

Salicylic acid chromogenic reaction, H_2O_2 (400 μL, 5 mM) and $FeSO_4$ (400 μL, 1.8 mM) were added to each tube, followed by PT, PT@CA, or MM@PT@CA (100 μL each). After 30 min of reaction, salicylic acid (100 μL, 1.8 mM) was added, and colorimetric analysis was performed to observe purple color formation, indicating Fe^{3+} generation.

Antibacterial Activity of MM@PT@CA

The antibacterial efficacies of the different components were evaluated against *Escherichia coli* (*E. coli*) and *Staphylococcus aureus*. (*S. aureus*). Bacterial suspensions were diluted to 1×10^7 CFU/mL and incubated with materials (Control, PT, PT@CA, MM@PT@CA and gentamicin) at a concentration of 2 mg/mL under constant agitation (200 rpm) at 37 °C. The optical density of the bacterial cultures was measured at predetermined time intervals to construct bacterial growth curves based on which the bacterial clearance ratio was calculated.

Following 6-hour co-incubation of *E. coli* and *S. aureus* with materials (Control, PT, PT@CA, MM@PT@CA), bacterial suspensions were serially diluted to 10^{-6} and plated on agar plates for colony counting.

$$\text{Bacterial clearance ratio}(\%) = \frac{C_{control} - C_{sample}}{C_{control}} \times 100\%$$

C_{control} and C_{sample} denote the number of colonies on agar plates from different groups.

Cytotoxicity and Hemolysis Assay of MM@PT@CA

Cytotoxicity assay: RAW264.7, cells were treated with PT, PT@CA, or MM@PT@CA nanoparticles. After 24 h of incubation, cell viability was assessed using the CCK-8 assay. Live/dead staining was performed using a fluorescence microscope for morphological evaluation. Cell viability was assessed in triplicate wells and repeated in three independent experiments (biological replicates, n = 3).

Hemolysis test: Equivalent concentrations of different samples were mixed with 2% red blood cell suspension. Negative (normal saline) and positive (deionized water) conditions were established in parallel. The mixtures were incubated at 37 °C for 0.5–3 h. Following centrifugation, the supernatant was transferred to 96-well plates and absorbance at 540 nm was measured using a microplate reader. The percentage of hemolysis was calculated using the following formula:

$$\text{Hemolysis ratio}(\%) = \frac{A_{\text{sample}} - A_{\text{negative}}}{A_{\text{positive}} - A_{\text{negative}}} \times 100\%$$

A_{negative} represents the sample-free group diluted with normal saline (0.9% NaCl), A_{sample} is the test sample group diluted with normal saline, and A_{positive} corresponds to the sample-free group diluted with deionized water.

Cellular Uptake of MM@PT@CA

Prior to membrane extraction, M2 macrophages were labeled with CD206 fluorescent antibody. The resulting fluorescently tagged macrophage membranes were used to coat micelles. These fluorescent MM@PT@CA nanoparticles were co-incubated with RAW264.7 cells for 6 hours. Cellular uptake was evaluated by cytoskeleton staining and subsequent fluorescence microscopy, which allowed the visualization of nanoparticle internalization by macrophages.

ROS Scavenging Activity of MM@PT@CA in Cells

RAW264.7 cells were seeded in 48-well plates at a density of 5×10^4 cells per well. After stimulation with 1 μg/mL LPS for 6 h, the cells were treated with PT, PT@CA and MM@PT@CA for an additional 24 h. Following the treatments, the culture medium was removed, and the cells were gently washed twice with PBS. Then, 5 μM DCFH-DA fluorescent probe was added and incubated with the cells at 37 °C in the dark for 30 min. After incubation, the cells were rinsed with PBS to remove any unincorporated probe. Subsequently, the nuclei were stained with 1 μg/mL DAPI solution, followed by PBS washes. Finally, the cells were observed and imaged using an inverted fluorescence microscope. The data are presented from three independent experiments (n = 3).

In Vitro Anti-Inflammatory Effects of MM@PT@CA

ELISA assay for inflammatory factors: RAW264.7 cells were seeded in 96-well plates at a density of 1×10^4 cells per well. The cells were stimulated with 1 μg/mL LPS for 6 h and then treated with PT, PT@CA and MM@PT@CA for an additional 48 h. A positive control (Dex) was additionally added. After the treatment, the culture supernatants were collected. The expression levels of four cytokines (TNF-α, IL-1β, IL-10, and Arg-1) were measured using commercial ELISA kits. The data are presented from three independent experiments (n = 3).

Detection of macrophage polarization: RAW264.7 macrophages (5×10^4 cells/well) were primed with LPS (1 μg/mL) for 6 h before 24-hour exposure to PBS or PT, PT@CA and MM@PT@CA. For fluorescence imaging, cellular monolayers were rinsed with PBS, fixed with 4% paraformaldehyde, and sequentially incubated with fluorophore-conjugated antibodies and DAPI nuclear stain, followed by microscopic examination after three PBS washes. The flow cytometry procedure involved

cell harvesting after treatment completion, ice-cold PBS washing, and 30-min incubation with fluorescent-tagged antibodies on ice. The washed cells were resuspended in chilled PBS for cytometric analysis, and signal quantification was performed using the FlowJo software. The data are presented from three independent experiments (n = 3).

In Vivo Therapeutic Efficacy of MM@PT@CA in SALI

All animal experimental procedures were approved by the Laboratory Animal Use and Management Committee of the General Hospital of Eastern Theater Command (Jinling Hospital, the Affiliated Hospital of Nanjing University Medical School) (Approval Number: DZGZRDW2400137). All experiments were performed in accordance with the Chinese National Standard GB/T 35892–2018 (Guidance for the Care and Use of Laboratory Animals). For procedures requiring anesthesia, mice were anesthetized by intraperitoneal injection of sodium pentobarbital (at a dose of 70 mg/kg). At the end of the experiment, euthanasia was performed by cervical dislocation under deep anesthesia. This method of euthanasia is consistent with and adheres to the recommendations of the Chinese National Standard GB/T 39760–2021 (Guidance for Euthanasia of Laboratory Animals).

Eight-week-old male C57BL/6 mice were used to establish a SALI model via cecal ligation and puncture (CLP). The CLP procedure was performed as follows: After anesthesia, mice were placed on a heating pad. The surgical site was shaved and disinfected with 75% alcohol. A midline abdominal incision approximately 1 cm in length was made with a scalpel. The peritoneal cavity was opened, and the cecum was identified and carefully exteriorized while avoiding damage to the mesenteric vessels. Approximately 50% of the cecum was ligated with a 6–0 silk suture to induce moderate sepsis. The ligated portion of the cecum was then punctured through with a 26-gauge needle, and a small amount of fecal content was extruded by gentle compression. The cecum was returned to the peritoneal cavity, and both the peritoneum and skin were closed in layers. To prevent shock, 1 mL of pre-warmed (37 °C) saline was administered subcutaneously. Mice were maintained on the heating pad until fully recovered from anesthesia before being returned to their cages. The specific experimental groups and dosing regimen are described in Table S1. At the experimental endpoint, mice were euthanized, and lung tissues were collected for subsequent analysis.

Histopathological assessment Lung tissues harvested following scheduled euthanasia were fixed in 4% PFA. After routine paraffin processing, 4-μm sections underwent to histomorphological analyses using H&E and Masson's trichrome staining, complemented by immunofluorescence and IHC evaluations.

Statistical Analysis

All experimental data were analyzed and plotted using Origin software. Statistical significance was determined by one-way analysis of variance (ANOVA) followed by Tukey's post-hoc test or Student's *t*-test, as appropriate for each dataset. Quantitative results are presented as the mean ± standard deviation (SD). Statistical significance levels are denoted as follows: $*p < 0.05$, $**p < 0.01$, and $***p < 0.001$.

Results and Discussion

Characterization of MM@PT@CA

Amphiphilic conjugate PT was synthesized by grafting TA onto PLL through an amide reaction. PT was dispersed in an aqueous solution and self-assembled into nanomicelles using the preparation process illustrated in Figure 2a. FTIR and ^{1}H NMR spectroscopy were employed to characterize the PT. FTIR spectra revealed a distinct C-S bond stretching peak at 647 cm^{-1} (Figure 2b), confirming the successful grafting of TA onto PLL. The ^{1}H NMR analysis in Figure 2c further validated this result: signals at 1.23–1.4 ppm corresponded to the alkane protons of TA (at the 2, 3, 4 positions), while peaks at 2.99–3.04 ppm were attributed to the protons in the five-membered ring of TA (at the 1 position).[23,24] In aqueous solutions, the hydrophobic segments of PT aggregate to form the micellar core to encapsulate hydrophobic drugs, while the hydrophilic segments constitute the outer shell. Following successful PT synthesis, CA was loaded into the PT micelles (PT@CA) via self-assembly. The existence of nanoparticles was observed through the Tyndall effect (Figure S1a), and the yield of PT@CA was 71.3%. Ultraviolet-visible spectroscopy confirmed the CA loading by detecting a characteristic absorption peak at 286 nm in PT@CA, which matched the CA standard (Figure 2d).[25] To enhance micelle targeting to

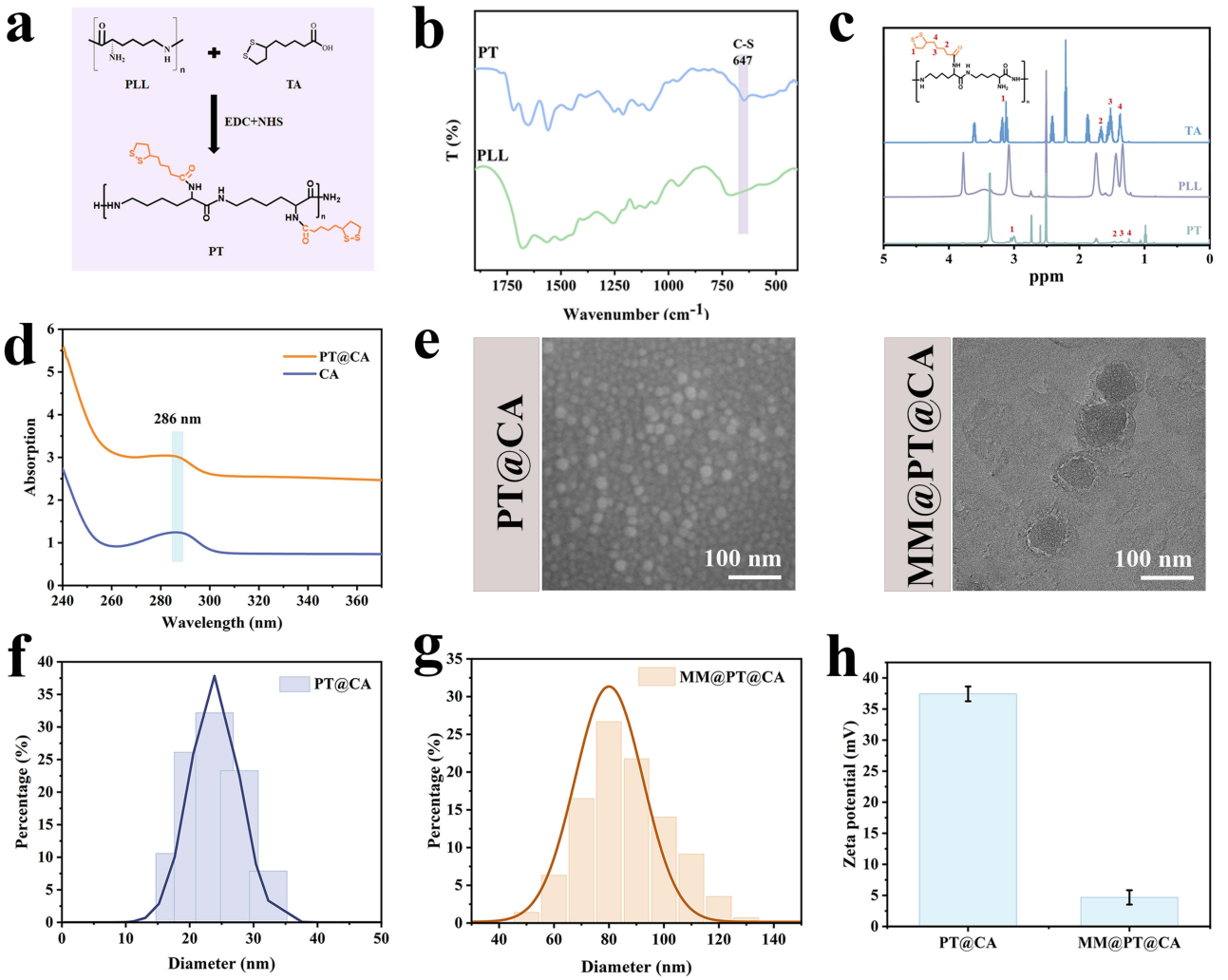

Figure 2 Characterization of MM@PT@CA. (**a**) Schematic illustration of amphiphilic monomer PT synthesis (**b**) FTIR spectra of PT and PLL. (**c**) ^{1}H NMR spectrum of TA, PLL and PT. The numbers (1, 2, 3, 4) indicate the assignment of the ^{1}H NMR signals to the corresponding protons in the PT structure. (**d**) UV–vis spectra of CA and PT@CA. (**e**) TEM images of PT@CA and MM@PT@CA. (**f**) Particle size distribution of PT@CA. (**g**) Particle size distribution of MM@PT@CA. (**h**) Zeta potentials of PT@CA and MM@ PT@CA.

inflammatory sites, PT@CA was cloaked onto M2 macrophage membranes (MM@PT@CA). TEM revealed spherical morphologies for both PT@CA (approximately 20 nm) and MM@PT@CA (approximately 80 nm) (Figure 2e), whereas fluorescence colocalization analysis confirmed the presence of CD206 membrane markers on the nanomicelles (Figure S2). DLS measurements showed that PT@CA had a hydrodynamic diameter of approximately 25 nm (Figure 2f), which is consistent with TEM observations. After extrusion through a 0.2 μm polycarbonate membrane during preparation, MM@PT@CA exhibited a diameter of approximately 80 nm (Figure 2g). Zeta potential analysis demonstrated that PT@CA carried a positive surface charge, which decreased after M2 membrane coating owing to the negatively charged membrane components (Figure 2h). These results collectively confirm the successful fabrication of MM@PT@CA nanomicelles with inflammation-targeting capabilities.

In Vitro Antioxidant Activity of MM@PT@CA

Under oxidative stress, disulfide bonds in TA are cleaved by ROS, triggering the release of CA with potent antioxidant activity from the hydrophobic core of the micelles. In vitro release assays were performed to evaluate the antioxidant performance of MM@PT@CA, in vitro release studies were conducted. On the basis of the standard curve regression equation for CA (Figure S1b), and the encapsulation efficiency of CA was 89.74%, drug loading of CA was 4.27%. As

shown in Figure 3a, MM@PT@CA exhibited a significantly higher cumulative release ratio in H_2O_2 solution than in PBS (more than twice that in PBS), confirming its ROS-responsive drug release behavior. The radical scavenging activity of MM@PT@CA was assessed using ABTS and DPPH assays. $ABTS^+$, a cationic radical, showed a maximum absorption at 734 nm, whereas the DPPH radical (with a single electron) displayed a strong absorption peak at 517 nm. The antioxidant capacity was quantified by monitoring the absorbance at these wavelengths. In the ABTS assay, the PT@CA and MM@PT@CA solutions appeared colorless and transparent (Figure 3b) with no absorption peak at 734 nm (Figure 3c), similar to the positive control. The ABTS radical scavenging ratio of MM@PT@CA was calculated to be 91.47% based on the absorbance values (Figure 3d). For the DPPH assay, the PT@CA solutions matched the positive control (yellow coloration), whereas MM@PT@CA retained a slightly purple hue (Figure 3e). Absorbance analysis revealed no peak at 517 nm for PT@CA, whereas MM@PT@CA exhibited a weak peak (Figure 3f), corresponding to a DPPH scavenging ratio of 74.07% (Figure 3g). Additionally, H_2O_2 scavenging efficacy was evaluated (Figure 3h). PT@CA achieved near-complete H_2O_2 elimination within 15 min, whereas MM@PT@CA achieved approximately 60% scavenging, which is comparable to PT, and attained its maximal scavenging capacity within 5 min. Different materials were incubated with Fe^{2+} and H_2O_2, followed by addition of salicylic acid for color development. The scavenging capacity of the materials toward H_2O_2 was evaluated by monitoring the formation of purple complexes. As shown in

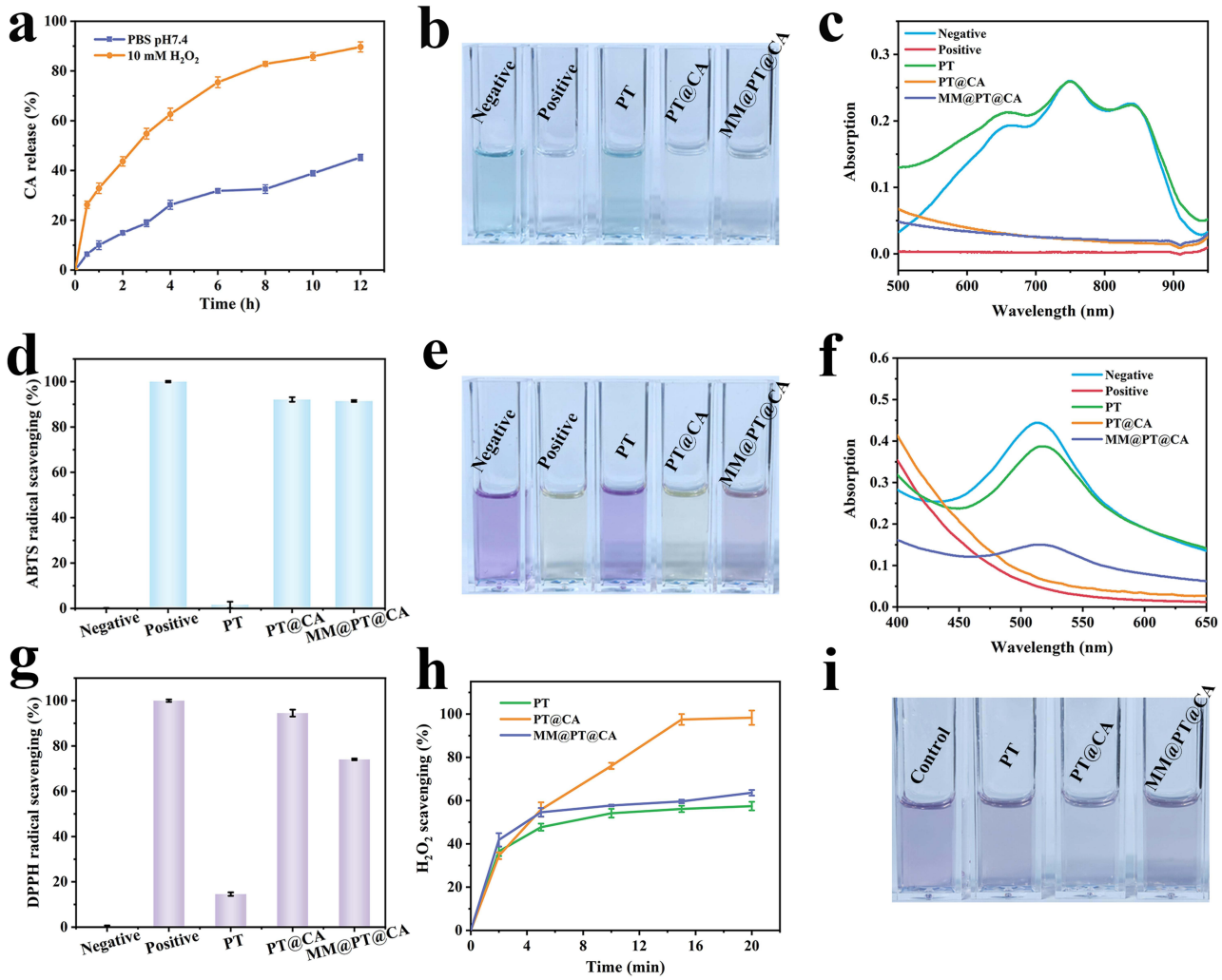

Figure 3 In vitro antioxidant activity of MM@PT@CA. (**a**) The in vitro release profile of MM@PT@CA. Photographic images (**b**), UV curves (**c**), and clearance ratio (**d**) of ABTS scavenging by PT, PT@CA, and MM@PT@CA. photographic images (**e**), UV curves (**f**), and clearance ratio (**g**) of DPPH scavenging by PT, PT@CA, and MM@PT@CA. (**h**) H_2O_2 scavenging ratio of PT, PT@CA, and MM@PT@CA. (**i**) Photographic images of the salicylic acid color reaction for PT, PT@CA, and MM@PT@CA.

https://doi.org/10.2147/IJN.S565422

Figure 3i, PT@CA effectively protected Fe^{2+} from oxidation and reduced the generation of purple complexes, indicating that PT@CA retained its antioxidant activity. Notably, although MM@PT@CA exhibited slightly reduced antioxidant activity compared with PT@CA, its unique membrane structure introduced an additional response mechanism, suggesting its potential advantages for targeted therapeutic applications.

Antibacterial Properties of MM@PT@CA

Bacterial infection is a key etiological factor in SALI,[26–28] and the use of antimicrobial agents to eliminate pathogens is critical for the treatment of SALI. To evaluate the antibacterial efficacy of MM@PT@CA, *E. coli* and *S. aureus* were co-incubated with MM@PT@CA for 18 h and bacterial growth curves were plotted by measuring the OD at specific intervals. As shown in Figures 4a and b, the PT@CA group consistently exhibited significantly lower OD values, indicating superior antibacterial activity. A clear divergence in OD values between PT@CA and PT/MM@PT@CA emerged at 6 hours post-incubation, though all three formulations (PT, PT@CA, and MM@PT@CA) demonstrated measurable antibacterial effects compared to the blank control.

After 6 h of co-incubation, the bacterial suspensions were diluted to 10^6 times and plated onto agar plates. Visual inspection of the agar plates (Figure 4c) revealed that PT@CA had the strongest antibacterial effect, showing no significant difference from the positive group. MM@PT@CA and PT followed, suggesting that the apoptotic cell membrane coating partially attenuated CA's antimicrobial potency of CA. Colony counting confirmed these observations; MM@PT@CA exhibited reduced bacterial clearance efficiency compared with PT@CA (Figure 4d). Notably, CA demonstrated higher sensitivity toward *S. aureus* than *E. coli*, with enhanced bactericidal efficacy against the former.[29] The antimicrobial mechanism of CA may be attributed to the lipophilic nature of phenolic compounds, which enables

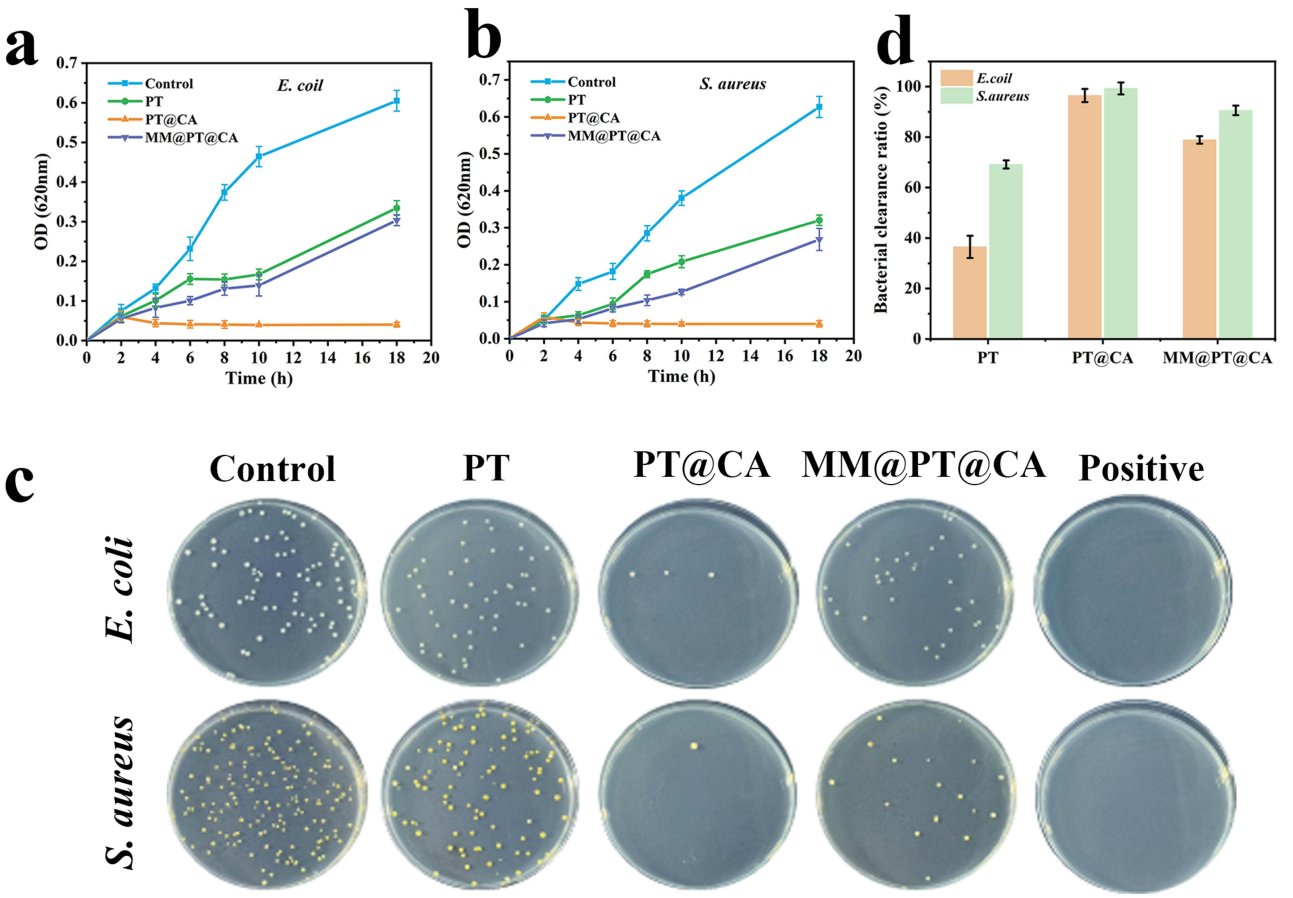

Figure 4 Antibacterial properties of MM@PT@CA. Bacterial growth curves of *E. coli* (**a**) and *S. aureus* (**b**) for PT, PT@CA, and MM@PT@CA. (**c**) Photographic images of PT, PT@CA, and MM@PT@CA agar plates. The Positive group was treated with gentamicin. (**d**) Bacterial clearance ratio of PT, PT@CA, and MM@PT@CA.

their penetration of bacterial cell membranes.[30] Within the membrane, hydrogen bond donor groups in CA are likely to interact with phosphorylated membrane components, disrupting structural integrity.[31,32] Collectively, these results validated the antibacterial potential of MM@PT@CA.

Cytotoxicity and Cellular Uptake of MM@PT@CA

A critical requirement for nanoparticles in nanomedicine is their excellent biocompatibility.[33] The hemolysis assay results demonstrated that the hemolysis ratios of PT, PT@CA, and MM@PT@CA were < 5% (Figure S3).To evaluate the cytotoxicity of MM@PT@CA, RAW264.7 cells were treated with different materials for 24 and 48 h. Live/dead staining fluorescence images (Figure 5a) combined with the CCK-8 assay results (Figure 5b) demonstrated that MM@PT@CA had no adverse effect on RAW264.7 the viability. Macrophages play a pivotal role in the inflammatory response in SALI.[34] To investigate macrophage uptake by the nanoparticles, the internalization of MM@PT@CA by RAW264.7, cells was observed using fluorescence microscopy. As shown in Figure 5c, MM@PT@CA was effectively internalized by macrophages after 6 h of co-incubation, and LPS-induced macrophages took up more MM@PT @CA than normal macrophages, demonstrating the inflammatory targeting of MM@PT@CA. Moreover, the morphology of the cytoskeleton indicated that MM@PT@CA did not compromise the cellular integrity. These results indicate the excellent biocompatibility of micellar materials.

MM@PT@CA Alleviates Oxidative Stress in Macrophages

The core pathological features of SALI include inflammatory cell recruitment and infiltration, dysregulation of inflammatory responses, and the disruption of redox homeostasis. During this process, excessive ROS generation forms a vicious cycle with persistent oxidative stress, which not only directly exacerbates tissue oxidative damage but also drives SALI progression through positive regulation of inflammatory cascades, representing a key molecular mechanism in SALI pathogenesis. LPS, a well-known PAMP, stimulates ROS production. Therefore, we evaluated the in vivo antioxidant effects of our material by measuring the LPS-induced ROS generation in cells. As shown in Figure 5d, LPS stimulation significantly increased ROS production, confirming the successful establishment of the in vitro inflammation model. Under these conditions, MM@PT@CA treatment effectively reduced ROS generation and alleviated oxidative stress damage in the cells. To further investigate the effects of MM@PT@CA on oxidative stress, we used H_2O_2 as a positive control to induce oxidative stress injury in RAW264.7 cells. Figure 5e presents the live/dead fluorescence staining images of cells treated with different materials following H_2O_2 induction. Compared to the model group, MM@PT@CA treatment significantly reduced oxidative stress-induced cell death. This protective effect was further confirmed by the CCK-8 assay results (Figure 5f), which demonstrated that MM@PT@CA treatment remarkably restored the cell viability.

MM@PT@CA Modulates Macrophage Polarization

Macrophages, as dynamic responders of the innate immune system, possess significant phenotypic plasticity, with their functional lineages being reprogrammable according to the spatiotemporal dynamics of the inflammatory microenvironments.[35] In this study, we observed that in the LPS-induced inflammation model, macrophages underwent classical M1 polarization, characterized by upregulated expression of signature markers CD86 and iNOS. Conversely, M2 macrophages counterbalance Th1 immune responses through elevated expression of anti-inflammatory molecules including Arg-1, CD206, and IL-10. By leveraging this homeostatic mechanism, intervention strategies targeting macrophage phenotype switching during the acute phase of SALI may provide immunomodulatory therapeutic approaches that disrupt the vicious cycle of inflammation and oxidative stress. Using an LPS-induced in vitro inflammation model, we assessed the M1/M2 marker expression using immunofluorescence and flow cytometry. As shown in Figures 6a–d, compared with the control group, LPS-stimulated RAW264.7, cells exhibited significantly increased M1 marker CD86 and decreased M2 marker CD206. Under LPS stimulation, both PT@CA and MM@PT@CA treatments effectively downregulated CD86 and upregulated CD206 expression compared to the PT group, demonstrating the ability of CA to modulate macrophage polarization. Flow cytometry results (Figure 6e) corroborated these findings: MM@PT@CA treatment reduced the $CD86^+$ population from 33.8% to 15.5% and increased $CD206^+$ cells from

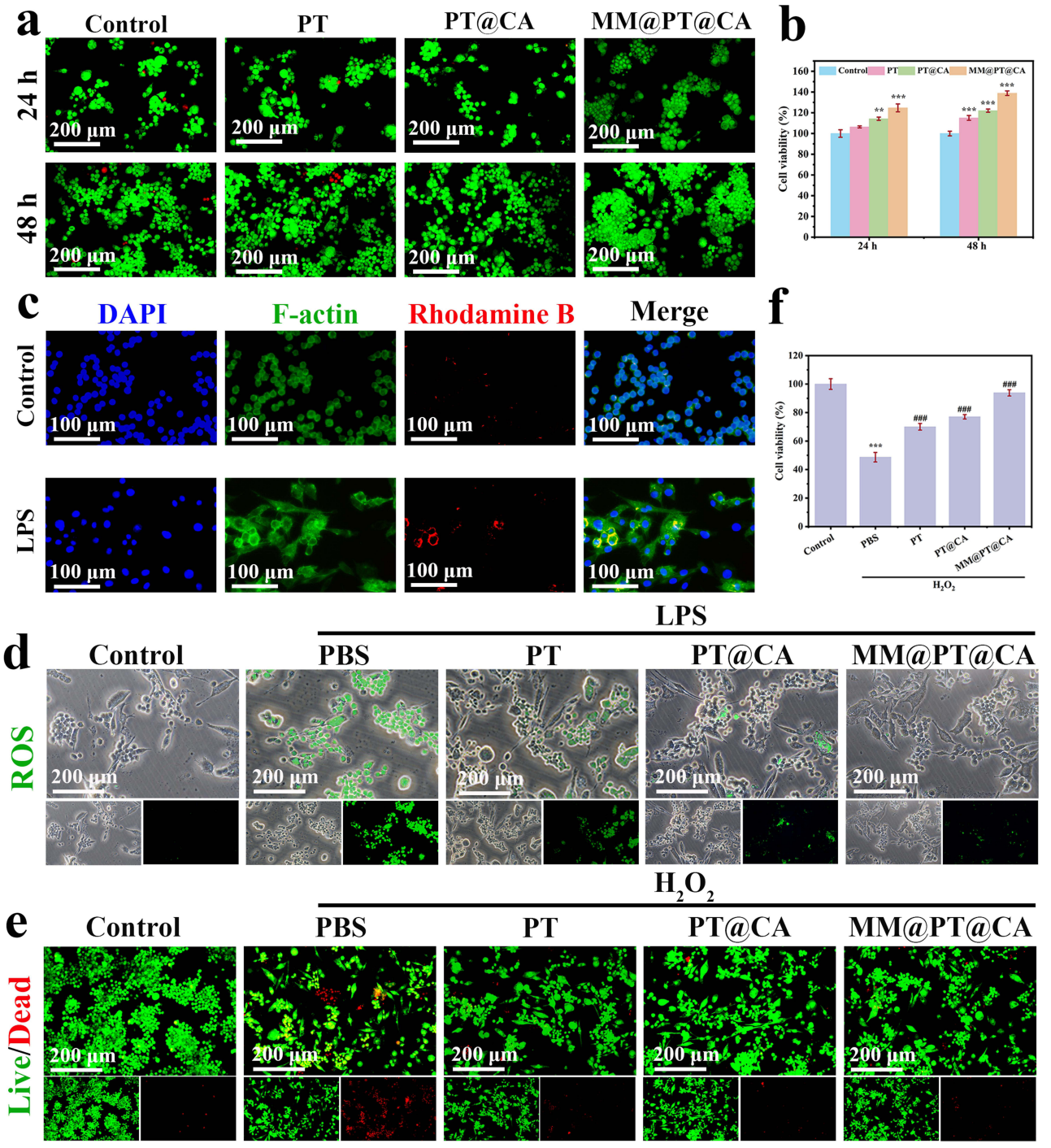

Figure 5 Biocompatibility and in vivo antioxidant properties of MM@PT@CA. (**a**) Live/dead fluorescence staining images of RAW264.7 cells co-cultured with different materials for 24 h and 48 h. (**b**) Cell viability determined by CCK-8 assay after 24 h and 48 h incubation with various materials. (**c**) Cellular uptake images following 6-hour co-incubation with MM@PT@CA. (**d**) Fluorescence images of ROS generation in LPS-stimulated cells treated with different materials. (**e**) Live/dead fluorescence staining images of cells after H_2O_2 stimulation with various material treatments. (**f**) CCK-8 results showing cell viability recovery after H_2O_2 stimulation with different material treatments. (**p<0.01, ***p<0.001 vs control; $^{\#\#\#}p$<0.001 vs PBS).

9.03% to 36.4% in LPS-stimulated macrophages, indicating a predominant M2 polarization. Furthermore, ELISA analysis of polarization-associated cytokines (Figures 6f–i) revealed that LPS stimulation significantly elevated IL-1β and TNF-α (M1 cytokines), while suppressing IL-10 and Arg-1 (M2 markers), compared to the control. Treatment with different materials (PT, PT@CA, and MM@PT@CA) progressively decreased M1 cytokine secretion and enhanced M2

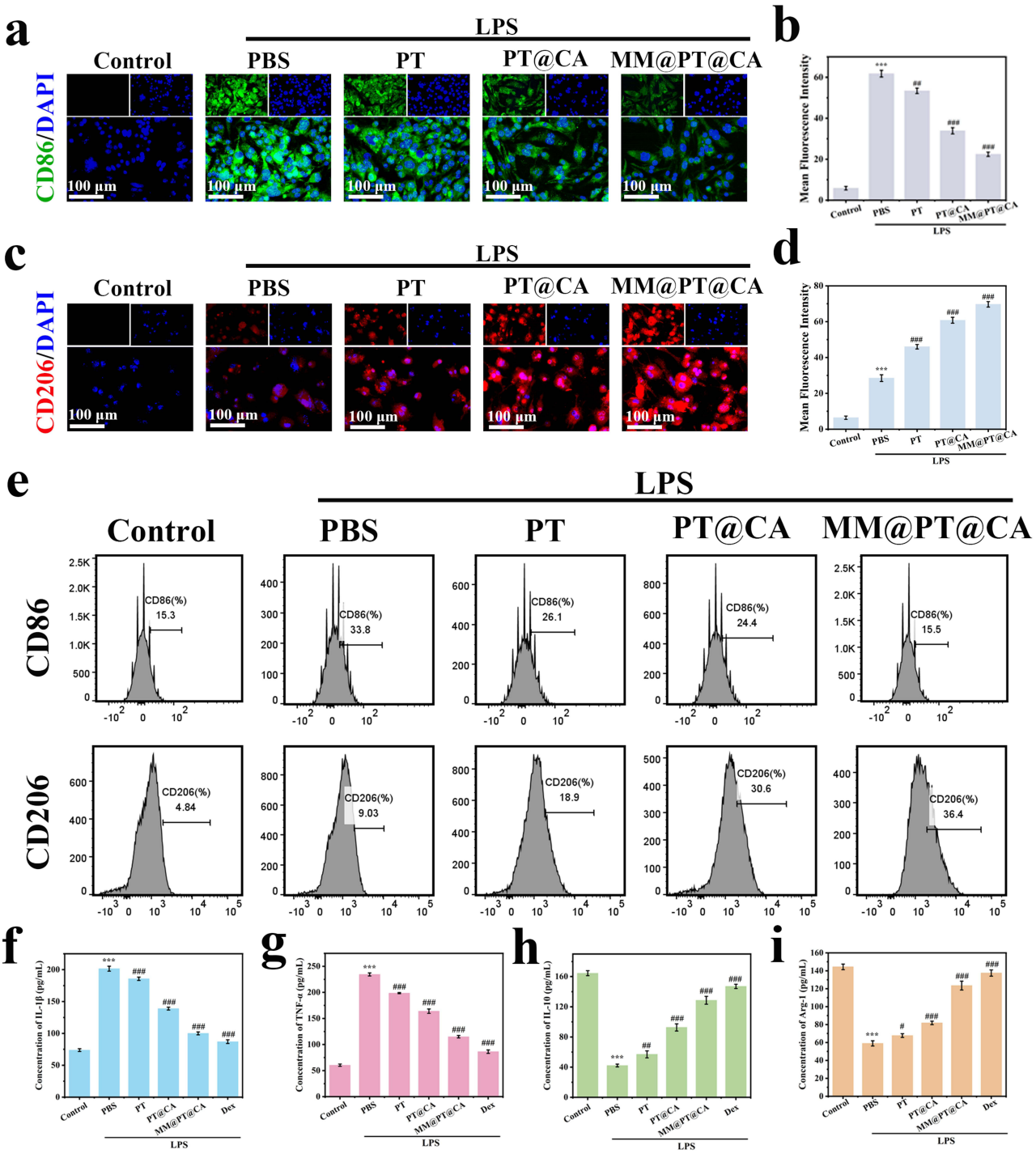

Figure 6 MM@PT@CA modulates macrophage polarization. (**a**) Immunofluorescence images of CD86 and (**b**) quantitative analysis. (**c**) Immunofluorescence images of CD206 and (**d**) quantitative analysis. (**e**) Flow cytometric analysis of macrophage polarization status. ELISA quantification of inflammatory cytokines: (**f**) IL-1β, (**g**) TNF-α, (**h**) IL-10, and (**i**) Arg-1 expression levels. The positive control was dexamethasone. (***p<0.001 vs control; $^{\#}p$<0.05, $^{\#\#\#}p$<0.01, $^{\#\#\#\#}p$<0.001 vs PBS).

cytokine production in LPS-stimulated macrophages. The effect of MM@PT@CA was comparable to that of the positive control (Dex). These results collectively demonstrate that CA (via PT@CA and MM@PT@CA) exerts anti-inflammatory effects by promoting macrophage repolarization toward the M2 phenotype.

https://doi.org/10.2147/IJN.S565422

MM@PT@CA Reduces Cellular Apoptosis and Maintains Pulmonary Structural Integrity

The SALI model was induced in mice using the CLP method. Lung tissues were collected for analysis at 24 hours post-procedure. Figure 7a shows a schematic of the SALI mouse model at 24-hour treatment. As shown in Figures 7b and c, the CLP model group (28.79%) exhibited significantly increased cellular apoptosis compared with the sham group, indicating substantial lung tissue damage. While PT treatment (17.2%) showed minimal effect on apoptosis reduction, both PT@CA (10.55%) and MM@PT@CA treatments (5.49%) markedly decreased the number of apoptotic cells, suggesting the effective mitigation of SALI. To further validate these findings, the lung tissue sections were subjected to H&E and Masson's trichrome staining. H&E staining (Figure 7d) revealed severe inflammatory cell infiltration in the CLP model group. MM@PT@CA (or PT@CA) treatment effectively suppressed inflammatory cell infiltration, which was consistent with their anti-inflammatory effects both in vivo and in vitro. Moreover, MM@PT@CA (or PT@CA) substantially restored the disrupted alveolar architecture, attenuated alveolar/interstitial hemorrhage and exudation, and reduced alveolar wall thickening. Masson staining results (Figure 7e) corroborated the H&E findings: The Sham group maintained an intact alveolar structure with a thin interstitium and perivascular blue collagen fibers, while the CLP model group showed significantly thickened alveolar septa with extensive interstitial collagen deposition (blue staining) and localized alveolar fusion. MM@PT@CA (and PT@CA) treatment resulted in thinner alveolar septa and reduced collagen deposition. These results collectively demonstrate that MM@PT@CA (or PT@CA) alleviates SALI by reducing cellular apoptosis and preserving the alveolar structural integrity.

MM@PT@CA Modulates Macrophage Polarization and Alleviates Pulmonary Inflammation

Systemic inflammation is a critical process in the pathophysiology of SALI and is primarily characterized by the pronounced activation of inflammatory cells and extensive release of pro-inflammatory cytokines.[36,37] Maintaining an optimal balance between the M1 and M2 macrophage phenotypes is essential for mitigating inflammatory responses under pathological conditions. Using immunofluorescence, we investigated the effects of MM@PT@CA on macrophage polarization, with M1 macrophages labeled with iNOS (green) and M2 macrophages identified by CD206 (red) staining (Figure 8a), followed by quantitative fluorescence intensity analysis (Figure 8b). The results demonstrated a predominant pro-inflammatory M1 polarization in the CLP group, whereas MM@PT@CA (or PT@CA) treatment promoted anti-inflammatory M2 polarization. Immunohistochemical examination of inflammatory factors (Figure 8c) and quantitative analysis (Figures 8d–g) revealed significantly elevated expression of TNF-α, MPO, MMP2 and MMP9 (brown-stained cells) in the CLP group compared to the sham controls. Although PT treatment exhibited modest anti-inflammatory effects relative to the CLP group, MM@PT@CA (or PT@CA) demonstrated superior efficacy, with the M2 cell membrane coating further enhancing therapeutic outcomes. MPO, secreted by activated neutrophils and monocytes, shows expression levels proportional to neutrophil infiltration.[38] MMP9, which is primarily released by inflammatory cells, can degrade the extracellular matrix when overexpressed, thereby facilitating deeper tissue infiltration by inflammatory cells.[39] In comparison, MMP2 also degrades the extracellular matrix but is predominantly sustained by structural cells like fibroblasts and endothelial cells, fulfilling a more foundational role in tissue remodeling. In pulmonary tissues, sepsis-induced inflammatory storms damage the basement membranes, with transient extracellular matrix deposition triggering increased MMP9 release, a process that is further amplified by TNF-α. The inflammatory environment concurrently activates MMP2.[40] Together, MMP2 and MMP9 work synergistically to enhance basement membrane disruption, facilitating the massive infiltration of inflammatory cells into the lung interstitium and alveoli.[41,42] These cells subsequently release more inflammatory mediators, worsening pulmonary injury. Collectively, MM@PT@CA alleviated SALI by reprogramming macrophages toward an anti-inflammatory phenotype, modulating inflammatory factor secretion, and reducing neutrophil infiltration.

In terms of biosafety, histopathological analysis of major organs preliminarily confirmed that MM@PT@CA did not induce significant toxic reactions or pathological damage in the heart, liver, spleen, lungs, or kidneys (Figure S4), indicating favorable biosafety. It should be noted that while this study accomplished proof-of-concept, advancing toward

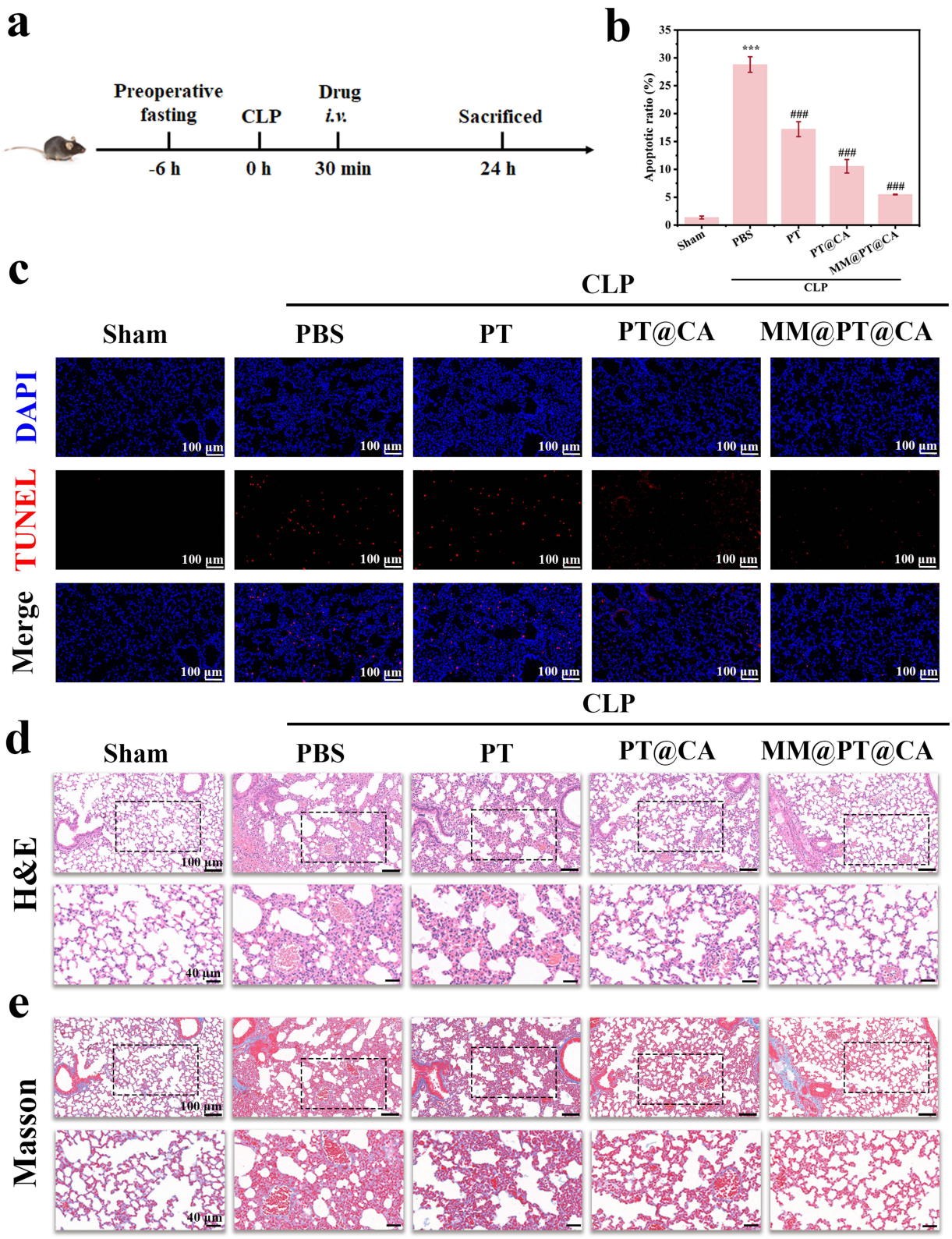

Figure 7 MM@PT@CA mitigates lung injury. (**a**) Schematic diagram of the experimental protocol. (**b**) Quantitative analysis of apoptotic cells in lung tissues by TUNEL staining. (**c**) Representative fluorescent images of TUNEL staining in lung tissue sections. (**d**) Histopathological evaluation by H&E staining of lung tissues. (**e**) Collagen deposition assessment by Masson staining of lung sections. (***p<0.001 vs control; $^{\#\#\#}p$<0.001 vs PBS. The magnification of the image in the first row is 20X, and that in the second row is 40X. The black dashed box represents the position of the 40X image within the 20X image, indicating the area that has been enlarged).

https://doi.org/10.2147/IJN.S565422

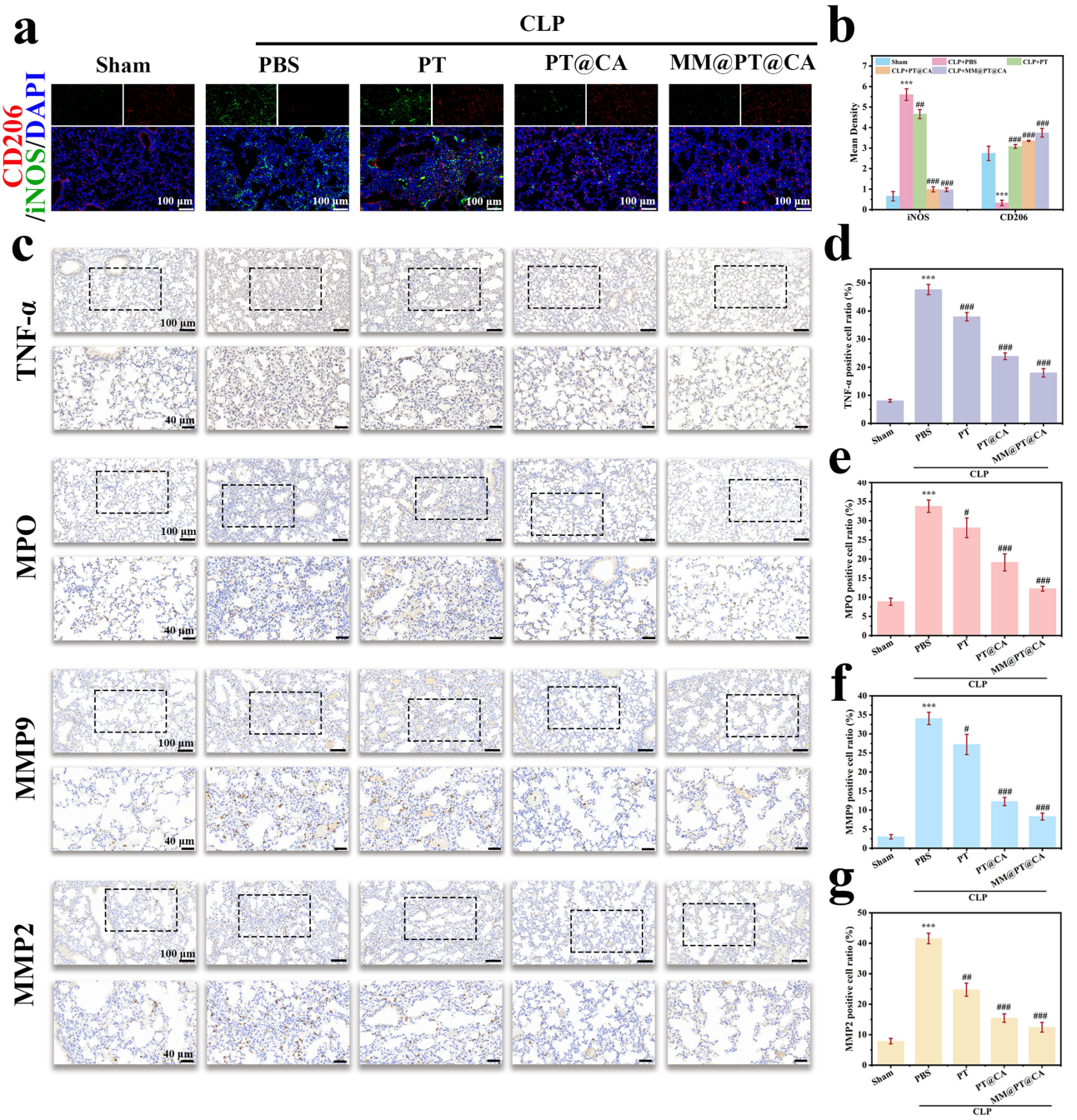

Figure 8 MM@PT@CA modulates macrophage polarization and alleviates pulmonary inflammation. (**a**) Immunofluorescence analysis of macrophage polarization status. (**b**) Quantitative analysis of macrophage polarization by immunofluorescence. (**c**) Immunohistochemical detection of inflammatory factors (TNF-α, MPO, MMP9, MMP2) expression. Statistical quantification of immunohistochemically positive cells for TNF-α (**d**), MPO (**e**), MMP9 (**f**) and MMP2 (**g**). (***p<0.001 vs control; $^{\#}p$<0.05, $^{\#\#}p$<0.01, $^{\#\#\#}p$<0.001 vs PBS. The magnification of the image in the first row is 20X, and that in the second row is 40X. The black dashed box represents the position of the 40X image within the 20X image, indicating the area that has been enlarged).

clinical translation still requires systematic evaluation of the following key parameters: the long-term pharmacokinetic profile of the nanocarrier, the potential immunogenicity of the macrophage membrane coating, and the scalability of the production process. These important issues will form the core focus of our subsequent research.

Conclusion

In this study, we engineered a biomimetic nanomicelle, MM@PT@CA, aimed at targeting pulmonary inflammation and effectively treating SALI through modulation of cellular redox balance. Our findings indicate that MM@PT@CA exhibits high yield, potent ROS responsiveness, high biocompatibility, and precise inflammation-targeting capability. The therapeutic effect of MM@PT@CA against SALI is attributed to the antioxidant and anti-inflammatory properties of CA, which not only reduce ROS generation at the source but also reprogram activated macrophages toward the anti-inflammatory M2 phenotype, leading to mitigation of inflammatory responses in lung tissue. However, this study has certain limitations: the specific signaling pathways underlying CA-mediated anti-inflammatory effects require further exploration. Moreover, challenges related to the clinical translation of MM@PT@CA—such as the scalability and immune compatibility of macrophage membranes, as well as the long-term pharmacokinetics of the nanomedicine—still need to be addressed. In conclusion, as a multifunctional nanodelivery platform, MM@PT@CA offers a promising translational strategy for the treatment of SALI through coordinated regulation of redox homeostasis and the immune microenvironment.

Data Sharing Statement

Data supporting the findings of this study are available from the corresponding author, Lili Ding, upon reasonable request.

Ethical Approval

This study was approved by the Laboratory Animal Use and Management Committee of the General Hospital of Eastern Theater Command (Jinling Hospital, the Affiliated Hospital of Nanjing University Medical School) (Approval Number: DZGZRDW2400137) and conducted in strict accordance with its guidelines. This study does not involve research on human tissue.

Funding

This work was supported by Suqian Sci&Tech Program (KY202209, K202405), Jiangsu High-level Hospital Pairing Assistance Research Initiative (JDBFSQ202510), General Project of Science and Technology Development Fund of Nanjing Medical University (NMUB20210295).

Disclosure

The authors declare no conflicts of interest in this work.

References

1. Sun B, Lei M, Zhang J, et al. Acute lung injury caused by sepsis: how does it happen? *Front Med*. 2023;10:1289194. doi:10.3389/fmed.2023.1289194
2. Wu C, Li H, Zhang P, et al. Lymphatic flow: a potential target in sepsis-associated acute lung injury. *J Inflamm Res*. 2020;13:961–968.10.2147/jir.S284090. doi:10.2147/JIR.S284090
3. Meyer NJ, Gattinoni L, Calfee CS. Acute respiratory distress syndrome. *Lancet*. 2021;398(10300):622–637.10.1016/s0140–6736(21)00439–6. doi:10.1016/S0140-6736(21)00439-6
4. Zampieri FG, Mazza B. Mechanical ventilation in sepsis: a reappraisal. *Shock*. 2017;47(1S Suppl 1):41–46. doi:10.1097/shk.0000000000000702
5. Mogensen TH. Pathogen recognition and inflammatory signaling in innate immune defenses. *Clin Microbiol Rev*. 2009;22(2):240–273. doi:10.1128/CMR.00046-08
6. Steinhagen F, Schmidt SV, Schewe JC, et al. Immunotherapy in sepsis - brake or accelerate? *Pharmacol Ther*. 2020;208.
7. Copaescu A, Smibert O, Gibson A, et al. The role of IL-6 and other mediators in the cytokine storm associated with SARS-CoV-2 infection. *J Allergy Clin Immunol*. 2020;146(3):518–534.e1.10.1016/j.jaci.2020.07.001. doi:10.1016/j.jaci.2020.07.001
8. Liu L, Lin L, Wang Y, et al. L-AP alleviates liver injury in septic mice by inhibiting macrophage activation via Suppressing NF-κB and NLRP3 inflammasome/caspase-1 signal pathways. *J Agric Food Chem*. 2024;72(15):8460–8475. doi:10.1021/acs.jafc.3c02781
9. Sun Z, Wang Y, Jin X, et al. Crosstalk between dysfunctional mitochondria and proinflammatory responses during viral infections. *Int J Mol Sci*. 2024;25(17):9206. doi:10.3390/ijms25179206
10. Xin Q, Zhang S, Sun S, et al. Multienzyme active nanozyme for efficient sepsis therapy through modulating immune and inflammation inhibition. *ACS Appl Mater Interfaces*. 2024;16(28):36047–36062. doi:10.1021/acsami.4c04994

11. Che D, Xiao Y, Zhang X, et al. Multifunctional integrated polyphenol-copper nanozymes for sepsis-induced acute liver injury via ameliorating endoplasmic reticulum stress and reprogramming inflammatory microenvironment. *Chem Eng J*. 2025;507:160293. doi:10.1016/j.cej.2025.160293
12. Phan-Xuan T, Breitung B, Dailey LA. Nanozymes for biomedical applications: multi-metallic systems may improve activity but at the cost of higher toxicity? *Wiley Interdiscip Rev Nanomed Nanobiotechnol*. 2024;16(4):e1981. doi:10.1002/wnan.1981
13. Huang Y, Zhan M, Sun H, et al. Electrosprayed core-shell microspheres co-deliver fibronectin and resveratrol for combined treatment of acute lung injury. *J Colloid Interface Sci*. 2025;686:498–508.10.1016/j.jcis.2025.01.249.
14. Tsai YF, Yang SC, Hsu YH, et al. Carnosic acid inhibits reactive oxygen species-dependent neutrophil extracellular trap formation and ameliorates acute respiratory distress syndrome. *Life Sci*. 2023;321:121334. doi:10.1016/j.lfs.2022.121334
15. Kalantar H, Sadeghi E, Abolnezhadian F, et al. Carnosol attenuates bleomycin-induced lung damage via suppressing fibrosis, oxidative stress and inflammation in rats. *Life Sci*. 2021;287:120059. doi:10.1016/j.lfs.2021.120059
16. Wang W, Huang Z, Huang Y, et al. Pulmonary delivery nanomedicines towards circumventing physiological barriers: strategies and characterization approaches. *Adv Drug Deliv Rev*. 2022;185:114309. doi:10.1016/j.addr.2022.114309
17. Jiang Y, Nie D, Hu Z, et al. Macrophage-derived nanosponges adsorb cytokines and modulate macrophage polarization for renal cell carcinoma immunotherapy. *Adv Healthc Mater*. 2024;13(20):e2400303. doi:10.1002/adhm.202400303
18. Nakkala JR, Duan Y, Ding J, et al. Macrophage membrane-functionalized nanofibrous mats and their immunomodulatory effects on macrophage polarization. *Acta Biomater*. 2022;141:24–38.10.1016/j.actbio.2021.12.026.
19. Zhu J, Lei Z, Tang Y, et al. Preparation, characterization, and antibacterial and antioxidant activities of caffeic acid grafted ε-polylysine. *Int J Biol Macromol*. 2025;292:139276. doi:10.1016/j.ijbiomac.2024.139276
20. Elmizadeh A, Goli SAH, Mohammadifar MA, et al. Fabrication and characterization of pectin-zein nanoparticles containing tanshinone using anti-solvent precipitation method. *Int J Biol Macromol*. 2024;260:129463. doi:10.1016/j.ijbiomac.2024.129463
21. Yang L, Li W, Huang Z, et al. Engineered macrophage membrane-coated nanoparticles for hepatic ischemia-reperfusion injury therapeutics. *Biomater Res*. 2025;29:0212.10.34133/bmr.0212.
22. Zhou R, Xue S, Cheng Y, et al. Macrophage membrane-camouflaged biomimetic nanoparticles for rheumatoid arthritis treatment via modulating macrophage polarization. *J Nanobiotechnol*. 2024;22(1):578.10.1186/s12951–024–02822–9. doi:10.1186/s12951-024-02822-9
23. Shen F, Zhong H, Ge W, et al. Quercetin/chitosan-graft-alpha lipoic acid micelles: a versatile antioxidant water dispersion with high stability. *Carbohydr. Polym*. 2020;234:115927. doi:10.1016/j.carbpol.2020.115927
24. Tan W, Zhang J, Mi Y, et al. Synthesis and characterization of α-lipoic acid grafted chitosan derivatives with antioxidant activity. *React Funct Polym*. 2022;172:105205. doi:10.1016/j.reactfunctpolym.2022.105205
25. Chatterjee S, Chakraborty P, Dutta S, et al. Formulation of carnosic-acid-loaded polymeric nanoparticles: an attempt to endorse the bioavailability and anticancer efficacy of carnosic acid against triple-negative breast cancer. *ACS Appl Bio Mater*. 2024;7(3):1656–1670. doi:10.1021/acsabm.3c01087
26. Su R, Zhang Y, Zhang J, et al. Nanomedicine to advance the treatment of bacteria-induced acute lung injury. *J Mater Chem B*. 2021;9(44):9100–9115.10.1039/d1tb01770e. doi:10.1039/D1TB01770E
27. Grousd JA, Rich HE, Alcorn JF. Host-pathogen interactions in gram-positive bacterial pneumonia. *Clin Microbiol Rev*. 2019;32(3). doi:10.1128/cmr.00107-18
28. Liu J, Chen Q, Liu S, et al. coli induced acute lung injury in mice via equilibrating ACE-AngII-AT1R and ACE2-Ang-(1-7)-Mas axis. *Life Sci*. 2018;208:139–148. doi:10.1016/j.lfs.2018.07.013
29. Mo CJ, Xu YQ, Feng Y, et al. Simultaneous preparation of water- and lipid-soluble antioxidant and antibacterial activity of purified carnosic acid from Rosmarinus offocnalis L. *Ind Crops Prod*. 2022;187:115448. doi:10.1016/j.indcrop.2022.115448
30. Cowan MM. Plant products as antimicrobial agents. *Clin Microbiol Rev*. 1999;12(4):564–582. doi:10.1128/cmr.12.4.564
31. Souza AB, de Souza MG, Moreira MA, et al. Antimicrobial evaluation of diterpenes from Copaifera langsdorffii oleoresin against periodontal anaerobic bacteria. *Molecules*. 2011;16(11):9611–9.10.3390/molecules16119611.
32. Ojeda-Sana AM, Repetto V, Moreno S. Carnosic acid is an efflux pumps modulator by dissipation of the membrane potential in Enterococcus faecalis and Staphylococcus aureus. *World J Microbiol Biotechnol*. 2013;29(1):137–44.10.1007/s11274–012–1166–3.
33. Khane Y, Albukhaty S, Sulaiman GM, et al. Fabrication, characterization and application of biocompatible nanocomposites: a review. *Eur. Polym. J*. 2024;214:113187.
34. Li J, Ma W, Tang Z, et al. Macrophage-driven pathogenesis in acute lung injury/acute respiratory disease syndrome: harnessing natural products for therapeutic interventions (Review). *Mol Med Rep*. 2025;31(1). doi:10.3892/mmr.2024.13381
35. Zhou S, Zhu Y, Wu Y, et al. New insights on metabolic reprogramming in macrophage plasticity. *Int Immunopharmacol*. 2025;157:114797. doi:10.1016/j.intimp.2025.114797
36. Chen X, Tang J, Shuai W, et al. Macrophage polarization and its role in the pathogenesis of acute lung injury/acute respiratory distress syndrome. *Inflamm Res*. 2020;69(9):883–895. doi:10.1007/s00011-020-01378-2
37. Cheng P, Li S, Chen H. Macrophages in lung injury, repair, and fibrosis. *Cells*. 2021;10(2):436. doi:10.3390/cells10020436
38. Nussbaum C, Klinke A, Adam M, et al. Myeloperoxidase: a leukocyte-derived protagonist of inflammation and cardiovascular disease. *Antioxid Redox Signal*. 2013;18(6):692–713.10.1089/ars.2012.4783. doi:10.1089/ars.2012.4783
39. Huang Y, Li G, Li D, et al. Ethyl caffeate alleviates inflammatory response and promotes recovery in septic-acute lung injury via the TNF-α/NF-κB/MMP9 Axis. *Phytomedicine*. 2025;141:156700. doi:10.1016/j.phymed.2025.156700
40. Wang Y, Wang L, Luo R, et al. Glycyrrhizic acid against mycoplasma gallisepticum-induced inflammation and apoptosis through suppressing the MAPK pathway in chickens. *J Agric Food Chem*. 2022;70(6):1996–2009. doi:10.1021/acs.jafc.1c07848
41. Davey A, McAuley DF, O'Kane CM. Matrix metalloproteinases in acute lung injury: mediators of injury and drivers of repair. *Eur Respir J*. 2011;38(4):959–970. doi:10.1183/09031936.00032111
42. Liang Y, Yang N, Pan G, et al. Elevated IL-33 promotes expression of MMP2 and MMP9 via activating STAT3 in alveolar macrophages during LPS-induced acute lung injury. *Cell Mol Biol Lett*. 2018;23:52.10.1186/s11658–018–0117–x. doi:10.1186/s11658-018-0117-x